A Robust Monte Carlo Model for the Extraction of Biological Absorption and Scattering *In Vivo*

Janelle E. Bender*, Karthik Vishwanath, Laura K. Moore, J. Quincy Brown, *Member, IEEE*,
Vivide Chang, *Student Member, IEEE*, Gregory M. Palmer, and Nirmala Ramanujam

Abstract—We have a toolbox to quantify tissue optical properties that is composed of specialized fiberoptic probes for UV-visible diffuse reflectance spectroscopy and a fast, scalable inverse Monte Carlo (MC) model. In this paper, we assess the robustness of the toolbox for quantifying physiologically relevant parameters from turbid tissue-like media. In particular, we consider the effects of using different instruments, fiberoptic probes, and instrument-specific settings for a wide range of optical properties. Additionally, we test the quantitative accuracy of the inverse MC model for extracting the biologically relevant parameters of hemoglobin saturation and total hemoglobin concentration. We also test the effect of double-absorber phantoms (hemoglobin and crocin to model the absorption of hemoglobin and beta carotene, respectively, in the breast) for a range of absorption and scattering properties. We include an assessment on which reference phantom serves as the best calibration standard to enable accurate extraction of the absorption and scattering properties of the target sample. We found the best reference–target phantom combinations to be ones with similar scattering levels. The results from these phantom studies provide a set of guidelines for extracting optical parameters from clinical studies.

Index Terms—Biomedical optical spectroscopy, diffuse reflectance, Monte Carlo (MC) methods, tissue diagnostics, turbid media.

I. INTRODUCTION

DIFFUSE reflectance spectroscopy in the UV–visible (UV-VIS) range can be used to quantitatively and noninvasively measure a tissue's physiological (hemoglobin saturation, total hemoglobin content, and absorber concentrations) and morphological parameters (nuclear size and cellular density) *in vivo*. Diffuse reflectance spectroscopy has a broad range of applications in cancer-related fields, as systematic and significant differences appear in the optical spectroscopic properties of malignant and nonmalignant tissues [1]–[8]. These differences enable diffuse reflectance spectroscopy to be used in applications such as margin assessment during core needle biopsy [9] and tissue diagnostics [7], [8], [10]. Similar spectroscopic techniques are also being explored for monitoring tumor response

to therapy [11]–[14], as changes in the tumor vasculature and oxygenation, and thus, optical properties are expected during the course of cancer therapy. Another area in which diffuse reflectance spectroscopy could be applied is in monitoring changes in tissue hemoglobin levels due to blood loss or fluid replacement [15], in order to help guide transfusions during surgery.

Optical spectroscopic methods have high chemical specificity due to the large number of molecules, including hemoglobin, that interact with light. Fiberoptic technology can be employed to measure spectra remotely and noninvasively from several millimeters deep within intact human tissue. In diffuse reflectance spectroscopy, the sample is illuminated and the intensity of backscattered light is measured as a function of wavelength, typically with a fiberoptic probe. The reflected intensity relates to the attenuation of light as it propagates through the sample, undergoing elastic scattering and absorption interactions. The absorption and scattering coefficients of the tissue can be extracted from the intensity of the reflected light via analytical approximation to the transport equation [3], [16], [17], empirical methods [5], [18]–[21], or with Monte Carlo (MC) modeling [22], [23]. Of these techniques, the MC method is considered to provide a "gold standard" for accurate calculations of absorbed, reflected, or transmitted light in a turbid medium. However, the MC technique operates in a forward fashion, by calculating the diffuse reflectance from a medium given its optical properties. This procedure is very time consuming, and therefore, impractical to use for interpreting experimental measurements.

As a solution to this problem, we have developed an inverse scalable MC model of light transport [22] to operate in an inverse fashion by using a scaling technique to speed up the forward calculations [23], [24]. The model is flexible in that it can model a wide range of optical properties, any well-defined probe geometry, and is computationally efficient via the use of scaling techniques. In this paper, we present the quantitative accuracy of extracting a wide range of optical properties from tissue-mimicking phantoms with our inverse MC model of reflectance under a variety of different experimental conditions and with different instruments and fiberoptic probes to assess the robustness and clinical utility of the algorithm. The quantitative accuracy of the extracted absorption and scattering coefficients was tested with single-absorber phantoms composed of hemoglobin or crocin. These single-absorber phantoms were also used for an assessment on which reference phantom serves as the best calibration standard to extract optical properties from target samples. Hemoglobin phantoms were used to test the clinical utility of the algorithm in extracting hemoglobin

TABLE I
ILLUMINATION AND COLLECTION PARAMETERS

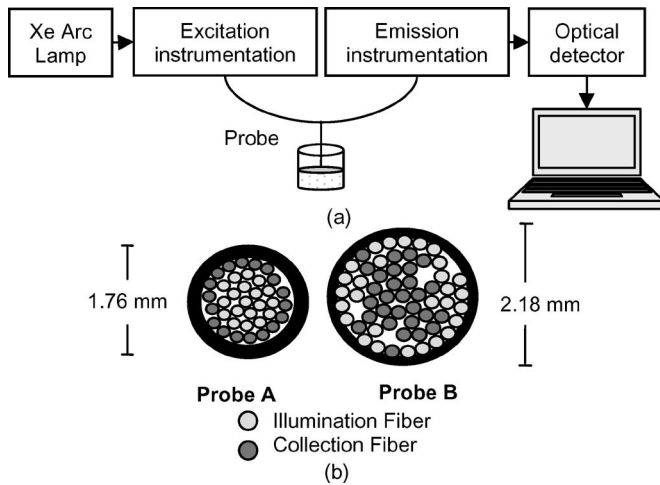|		INSTRUMENT A	INSTRUMENT B
Illumination Spectrometer	*Setting*	0-order	Synchronous with detection
	Bandpass (Slit Width)	(1 mm)	2.1 nm(0.5 mm)
	Grating	1200 grooves/mm	1200 grooves/mm
Collection Spectrometer and Detector	*Bandpass (Slit Width)*	1.9 nm(0.6 mm) or 10 nm(1 mm)	3.5 nm(0.5 mm)
	Grating	600 grooves/mm or 300 grooves/mm	1200 grooves/mm
	Sampling every	0.13 or 0.26 nm	5 nm
	Spectral range	350-600 nm	350-600 nm

Fig. 1. (a) Generalized schematic of the instruments used. (b) Schematic of the probes used.

saturation and total hemoglobin for a large range of concentrations. To model breast tissue, double-absorber phantoms (hemoglobin and crocin) were used to test the accuracy in extracting information about multiple absorbers using single-absorber reference phantoms.

II. MATERIALS AND METHODS

A. Instruments and Probes

Two different instruments designed to make diffuse reflectance measurements through a fiberoptic probe were tested. Fig. 1(a) shows a general representation of the instruments, and Fig. 1(b) shows a schematic representation of the common arm (in contact with the sample) for the two probes employed in the experiments described here. *Instrument A* used a 450-W Xe arc lamp (JY Horiba) filtered via a scanning double-excitation monochromator (Gemini 180, JY Horiba) as the source, while the remitted light was coupled through an imaging spectrograph (Triax 320, JY Horiba) and detected by a Peltier-cooled open-electrode charge-coupled device (CCD) (Symphony, JY Horiba). *Instrument B* (SkinSkan, JY Horiba) consisted of a 150-W Xe arc lamp and double-grating excitation monochromator as the source, while the reflected light was collected via an emission monochromator, and delivered to an extended red photomultiplier tube (PMT). For both instruments, the illumination and collection light was coupled to the tissue phantom via a bifurcated fiberoptic probe bundle.

Probe A (RoMack, Inc., Williamsburg, VA) used a core of 19 fibers for illumination and detected the reflected signal through an 18-fiber collection ring. Each individual optical fiber in the bundle had a core diameter of 200 μm with numerical aperture (NA) of 0.22. *Probe B* (RoMack, Inc.) consisted of 29 illumination fibers arranged around 29 collection fibers. The illumination fibers had NA of 0.125, while the collection fibers had NA of 0.12. The core/cladding diameter of each individual fiber in probe B was 200/245 μm. Both probes were custom-designed in-house. Probe geometry in each case was accounted for in the MC model via convolution over all illumination and collection

fibers. The centers of all illumination and collection fibers were determined by imaging the common end of the fiber bundle and calculating the coordinates of the illumination and collection centers using ImageJ [25]. The probe geometry was then integrated for every illumination–collection pair to determine collection probability [22].

B. Optical Measurements

The instrument settings for instruments A and B are tabulated in Table I.

The fixed parameters for instrument A were the CCD analog-to-digital conversion (ADC) gain (which was set to 6.7$\times$) and its ADC speed (which was set to 20 kHz). CCD gain is defined as the number of electrons generated in the CCD required to generate a single ADC count reported by the detector system. A 1200-grooves/mm grating and 1-mm slit widths were used for the illumination spectrometer. The spectral bandpass of the imaging spectrograph was fixed at 1.9 nm using a 600-grooves/mm grating and 0.6-mm slit width unless otherwise noted. The other spectral bandpass that was tested was fixed at 10 nm using a 300-grooves/mm grating and 1-mm slit width. Bandpass was calculated by measuring the emission spectrum from a krypton gas emission lamp (90-0014-01, UVP, Upland, CA) under the same experimental parameters used for the phantoms. The full-width at half-maximum of the lamp spectrum was determined from the 645.6 nm spectral line. Zero-order illumination was used, and the diffuse reflectance was collected over the wavelength range in 0.13 or 0.26 nm increments, depending on the grating used. For the 1.9-nm spectral bandpass setting, a 600-grooves/mm grating blazed at 400 nm was used to collect two scans with an approximately 10 nm overlap to cover the entire wavelength range. The first scan was from 348.5 to 479.9 nm, and the second scan was from 470.3 to 600.1 nm. The two scans were combined in postprocessing in MATLAB (The MathWorks, Natick, MA). To combine the spectra, the two scans were averaged in the region of overlap, beginning with the pixel of closest overlap. For the 10-nm spectral bandpass setting, a 300-grooves/mm grating blazed at 500 nm was used to collect a single scan that covered 334.9–602.1 nm.

The fixed parameters for instrument B were the excitation and emission bandpasses, which were fixed at 5 nm and the PMT

high voltage, which was set at 350 V. The spectral bandpass of the illumination and collection ends of instrument B was fixed at 2.1 and 3.5 nm, respectively, using 1200-grooves/mm excitation and emission monochromator gratings, and 0.5 mm slit widths. The bandpass of the collection end was calculated by measuring the emission spectrum from an He–Ne laser in the same manner as described earlier. The diffuse reflectance was measured using synchronous scanning over the wavelength range in 5 nm increments. A 1200-grooves/mm grating blazed at 350 nm was used to collect a single scan that covered 350–600 nm. Cubic splines were used to resample the spectra to 350–600 nm in increments reflective of the bandpass of the instrument. Dark subtract was enabled on both instruments to account for the noise from the dark signal. The reflectance from each phantom was measured once with the room lights off, and diffuse reflectance was collected. The exposure time of the initial phantom in a set was adjusted to reach a maximum SNR (at 500 nm) of greater than 100 for instrument A and instrument B. Phantom preparation and optical properties are described in Section II-D.

C. MC Model of Reflectance

The inverse MC model is based on a scaling approach described previously [24]. The diffuse reflectance from a single-baseline MC simulation for a given set of absorption and scattering coefficients (optical properties) is scaled using simple analytical expressions to predict the diffuse reflectance for any combination of optical absorption and scattering; these are compiled to create a lookup table for a wide range of absorption and scattering [22]. The inverse MC model we employed uses a flexible convolution scheme that accurately accounts for the fiber-probe geometry used in the experimental measurements by convolving the photon collection probability over each source–detector separation [22].

1) Fixed and Free Parameters of Fit: The diffuse reflectance spectrum is a function of the wavelength-dependent absorption and scattering coefficients that, in turn, are determined by specified absorber concentrations, scatter size, and scatter density [22]. The free parameters that are iteratively updated during the reflectance fitting include the absorber concentration and the scatterer size and volume density. The extinction coefficients for the absorber and the wavelength-dependent refractive indexes of the scatterer and surrounding medium are fixed parameters [22]. The average refractive indexes for the scatterer (polystyrene spheres) and surrounding medium (water) over 350–600 nm were 1.60 and 1.34, respectively. The refractive index of polystyrene spheres has been reported to be constant within approximately 1% of this value over the wavelength range used [26]. The extinction coefficients for oxy-Hb (HbO$_2$), deoxy-Hb (HbH), and crocin (Cr) were measured using a standard UV-VIS spectrophotometer (Cary 300, Varian, Inc., Palo Alto, CA).

2) Reference Phantom: In order to calibrate for system throughput and wavelength dependence, the measured diffuse reflectance spectrum from the sample is calibrated to the diffuse reflectance spectrum from a reference phantom with known optical properties. The reflectance spectrum of the reference phantom can be modeled by the MC algorithm using the scaling method. A ratio of the measured reference phantom reflectance to the modeled reference phantom reflectance gives a calibration factor that enables a direct comparison between measured and predicted reflectance spectra during the inversion process. When a reference phantom measurement from one day is used to calibrate for a sample measurement from a different day, an additional calibration step is carried out. The diffuse reflectance spectrum is measured from a reflectance standard, such as a spectralon puck (SRS-99-010, Labsphere, Inc., North Sutton, NH) or an integrating sphere immediately after the measurement to calibrate for day-to-day variations in system throughput. The use of different day reference–target inversions enabled us to mimic what is done in a clinical situation, where it is not practical to measure diffuse reflectance from a reference phantom.

3) Inversion Process: Given an experimentally measured diffuse reflectance spectrum, the inverse MC model minimizes the sum of squares error between the predicted diffuse reflectance and the measured diffuse reflectance by iteratively updating the optical properties. When the sum of squares difference between the modeled and measured diffuse reflectance is minimized, the concentrations of absorber(s) and the scatterer size and volume density that best predict the measured diffuse reflectance spectrum are extracted. We used 100 fits to ensure a stability of convergence.

D. Phantom Preparations

The first portion of phantom experiments tested the quantitative accuracy of the inverse MC model for extracting scattering and absorption coefficients using three sets of single-absorber phantoms. The accuracy in optical properties for the single-absorber phantom inversions was assessed using all reference and target phantom combinations within the same experiment. From the single-absorber phantom results, the best reference phantoms were selected. These reference phantoms were used to test the effect of spectral bandpass with instrument A and the effect of different instruments and probes. These reference phantoms were also used to test the algorithm's ability to extract absorber concentrations from two sets of biologically relevant phantoms: Hb saturation phantoms and phantoms with a large range of Hb concentrations. We then tested the robustness of the algorithm in extracting the concentrations of multiple absorbers in a double-absorber phantom set, using the best reference phantoms, which were measured on a different day.

Liquid tissue-simulating phantoms were prepared by mixing predetermined volumes of absorber with scatterer. Suspensions of 1-μm-diameter monodisperse polystyrene microspheres (07310, Polysciences, Inc., Warrington, PA) with known volume density were used as the scatterer. Powdered forms of human hemoglobin A$_0$ (H0267 ferrous stabilized, Sigma Co., St. Louis, MO) and/or crocin (17304 standard Fluka, Fluka, Allentown, PA) were used as the absorbers. Concentrated stock solutions of Hb (114 μM) and/or Cr (12.3 mM) were prepared by dissolving a known weight of the dry powders in deionized (DI) water and its absorption spectrum determined by measuring a

TABLE II
ABSORBER (HB) AND SCATTERER LEVELS USED IN SA_HB_A AND SA_HB_B

	Absorber levels				Scatterer levels	
	μ_a range (cm^{-1})	Mean μ_a (cm^{-1})	Hb (μM)		μ_s' range (cm^{-1})	Mean μ_s' (cm^{-1})
A1	0.01 - 0.80	0.2	0.7	S1	7.5 - 11.0	9.9
A2	0.08 - 7.1	1.5	6.4	S2	11.2 - 16.5	14.9
A3	0.11 - 10.4	2.2	9.2	S3	14.9 - 22.1	19.9
A4	0.14 - 12.8	2.7	11.4	S4	18.6 - 27.6	24.8
A5	0.17 - 15.9	3.3	14.2	S5	22.4 - 33.1	29.7

TABLE III
ABSORBER (CR) LEVELS USED IN SA_CR

Absorber levels			
μ_a range (cm^{-1})	Mean μ_a (cm^{-1})	Crocin (μM)	Fraction of A2
0.002 - 2.2	0.8	123.1	0.5
0.003 - 3.3	1.2	184.5	0.75
0.004 - 4.4	1.6	246.8	1
0.005 - 5.5	2	308.5	1.25

All four absorber levels were used for scatterer levels S2, S3, and S4.

diluted sample in a spectrophotometer. We used Hb and Cr as the absorbers since they simulate blood and beta-carotene, two of the absorbing species commonly present in breast tissues [27], which our group has studied extensively. The reduced scattering coefficient of the stock scatterer was determined from the Mie theory using freely available software [28], given the known size, density, and refractive index of the polystyrene spheres, as well as the refractive index of the surrounding medium. The phantoms were prepared and measured from 2.5-cm-diameter cylindrical plastic containers by diluting a small volume of the absorption stock solution with the scatterer and DI water to a total initial volume of 8 mL. The ratios of stock solution and scatterer volume to the total phantom volume enabled us to calculate the expected absorption (μ_a) and reduced scattering (μ_s') coefficients of the prepared phantom. For all prepared phantoms, the expected optical properties were comparable to the known absorption and scattering coefficients reported for human breast tissues in the UV-VIS wavelength range [29]. Reported averages in μ_a and μ_s' were taken over the 350–600 nm wavelength range.

1) Single-Absorber Phantoms: Three sets of single-absorber phantoms were used to test the accuracy of the inverse MC algorithm in extracting μ_a and μ_s'. Each phantom set "SA_Hb_a" and "SA_Hb_b" had Hb as the absorber, where either Hb or polystyrene spheres was added incrementally (SA_Hb_a and SA_Hb_b, respectively), while "SA_Cr" had Cr as the absorber. Each of SA_Hb_a and SA_Hb_b consisted of ten phantoms with absorber (Hb) and scatterer levels shown in Table II. Two containers were used for SA_Hb_a, each corresponding to an initial absorber level (A1) for a set scattering level (S2 and S4). The stock Hb solution was incrementally added to each container to increase the absorption coefficient from A1 to A5. Similarly, two containers were used for SA_Hb_b, each corresponding to an initial scattering level (S1) for a set absorber level (A2 and A4). Polystyrene spheres were incrementally added to each container to increase the scattering coefficient from S1–S5. Between each addition of absorber in SA_Hb_a or scatterer in SA_Hb_b, the reflectance spectrum was measured. The incremental additions of absorber in SA_Hb_a caused the scattering coefficients to decrease due to dilution by up to 12%, while the additions of scatterer in SA_Hb_b caused a dilution of the absorption coefficient up to 23%. These changes in the absorption and scattering coefficients were appropriately accounted for in subsequent calculations of the expected absorption and scattering coefficients.

SA_Cr consisted of 12 phantoms with absorber (Cr) levels shown in Table III. Three containers were used for SA_Cr, each

corresponding to an initial scattering level (S2–S4). The stock Cr solution was incrementally added to each container to increase the absorption coefficient. The magnitude of the absorption coefficients in SA_Cr was selected to be fractions of the A2 level (see Table II) in phantom sets SA_Hb_a and SA_Hb_b. The addition of absorber caused the scattering coefficient to decrease by 2% for each scattering level.

2) Hb Saturation Phantoms: In order to evaluate the extraction accuracy of Hb saturation, an experiment was conducted where concurrent optical and percent oxygen measurements were taken, while a phantom was deoxygenated over a 1-h time period. The gradual deoxygenation was accomplished via the addition of a small amount of Baker's yeast. A subset of phantoms from SA_Hb_a consisting of the five absorber levels for the S2 scattering level was used as reference for the deoxygenated phantom. The phantom used for deoxygenation had absorption and scattering coefficients corresponding to levels A5 and level S2 (see Table II), respectively. Phantoms in this set, "Sat_Hb," were buffered in $10\times$ PBS to keep the pH constant (pH = 6.94). Optical measurements were taken approximately every minute. The temperature in the room was regulated at 24 $^{\circ}$C. The phantom was continuously stirred to ensure uniform deoxygenation by the yeast. Hemoglobin saturation ($100[HbO_2]/([HbO_2] + [HbH])$) was calculated from the extracted concentrations of HbO_2 and HbH using reference phantoms measured on the same day.

The percent oxygen over the course of the optical measurements was independently and continuously monitored by an oxygen-sensitive electrode (MI-730, Microelectrodes, Inc., Bedford, NH). Prior to taking measurements, the electrode was calibrated in an air-saturated water sample, and a water sample completely deoxygenated by the addition of the reducing agent sodium dithionite ($Na_2S_2O_4$). The percent oxygen measured by the electrode was recorded at the beginning and end of each optical measurement and averaged for that time point. Oxygen partial pressure was determined from the percent oxygen measured by the electrode assuming a linear relationship. Expected saturation measurements were derived using the subroutine reported by Kelman [30]. The partial pressure of CO_2 was derived from the percent CO_2 in ambient air. For quantifiable comparison, values for the Hill's coefficient (n) and the partial pressure of oxygen at which Hb is 50% saturated (p_{50}) were calculated.

3) Hb Concentration Phantoms: A set of phantoms with Hb concentrations ranging from 1 to 35 μM was constructed to test the sensitivity and accuracy of our inversion model in extracting total Hb over a large range of concentrations, to model the variability in absorber concentrations seen in biological systems. One container was used for this phantom set, "Conc_Hb," in

TABLE IV
ABSORBER (HB) AND SCATTERER LEVELS USED IN CONC_HB

Phantom	μ_a range (cm^{-1})	Mean μ_a (cm^{-1})	Hb (μM)	μ_s' range (cm^{-1})	Mean μ_s' (cm^{-1})
H1	0.01 − 1.2	0.25	1.0	18.8 - 27.4	24.6
H2	0.03 − 2.7	0.57	2.3	18.6 - 27.1	24.3
H3	0.05 − 4.1	0.84	3.4	18.4 - 26.8	24.1
H4	0.07 − 5.5	1.14	4.6	18.2 - 26.5	23.8
H5	0.08 − 6.9	1.44	5.8	18.1 - 26.2	23.6
H6	0.1 − 8.3	1.73	7.0	17.9 - 25.9	23.3
H7	0.1 − 9.7	2.01	8.1	17.7 - 25.7	23.1
H8	0.1 − 11.0	2.29	9.2	17.5 - 25.4	22.8
H9	0.2 − 12.5	2.59	10.4	17.3 - 25.1	22.6
H10	0.2 − 13.9	2.89	11.6	17.1 - 24.8	22.3
H11	0.2 − 16.7	3.46	13.9	16.7 - 24.3	21.8
H12	0.2 − 19.4	4.03	16.2	16.3 - 23.7	21.3
H13	0.3 − 22.2	4.60	18.5	16.0 - 23.2	20.8
H14	0.3 − 25.1	5.20	20.9	15.6 - 22.6	20.3
H15	0.3 − 27.9	5.79	23.3	15.2 - 22.0	19.8
H16	0.4 − 35.0	7.25	29.2	14.2 - 20.6	18.5
H17	0.5 − 42.0	8.71	35.0	13.2 - 19.2	17.3

TABLE V
ABSORBER (CR AND HB) LEVELS USED IN DA_HBCR

Hb level A2				Hb level A4			
μ_a range (cm^{-1})	Mean μ_a (cm^{-1})			μ_a range (cm^{-1})	Mean μ_a (cm^{-1})		
	Total	Hb	Cr		Total	Hb	Cr
0.08 - 7.8	1.61	1.61	0	0.14 - 13.9	2.86	2.86	0
0.07 - 9.2	2.36	1.59	0.76	0.14 - 16.2	4.12	2.81	1.29
0.07 - 10.0	2.73	1.59	1.14	0.14 - 17.4	4.74	2.79	1.94
0.08 - 10.7	3.11	1.58	1.52	0.14 - 18.6	5.37	2.77	2.59
0.08 - 11.4	3.48	1.57	1.90	0.14 - 19.7	6.00	2.75	3.24

Each of the absorber levels was tested for two scattering levels (S2 and S4).

which the initial scattering level was approximately equal to S4 (see Table II). The phantoms in Conc_Hb spanned a larger range of absorption coefficients (H1–H17) than the phantoms in SA_Hb_a and SA_Hb_b, as shown in Table IV. Sequential addition of the absorber caused dilutions in the scattering coefficient by up to 30%. Phantoms measured on the same day, within the same set, were used as references for this set of phantoms.

4) Double-Absorber Phantoms: A set of 20 double-absorber (Hb and Cr) phantoms was used to test the algorithm's ability to extract concentrations of multiple absorbers, which more closely mimics breast tissue absorption properties. Each of the four containers used in this phantom set, "DA_HbCr," corresponded to an initial scattering and Hb absorption level. The first phantom in each container contained Hb as the only absorber. There were four combinations of scattering levels and initial Hb levels: A2–S2, A2–S4, A4–S2, and A4–S4 (see Table II). For each of these combinations, the stock Cr solution was added incrementally to yield four Cr absorber levels. The Cr levels were designed as fractions of the initial Hb level. The ranges of the absorbers are shown in Table V. As before, changes in the expected values of the scattering and absorption coefficients were accounted for in the prepared phantoms.

III. RESULTS

A. Single-Absorber Phantoms

We first tested the quantitative accuracy for extracting μ_a and μ_s' with phantom sets SA_Hb_a, SA_Hb_b, and SA_Cr using

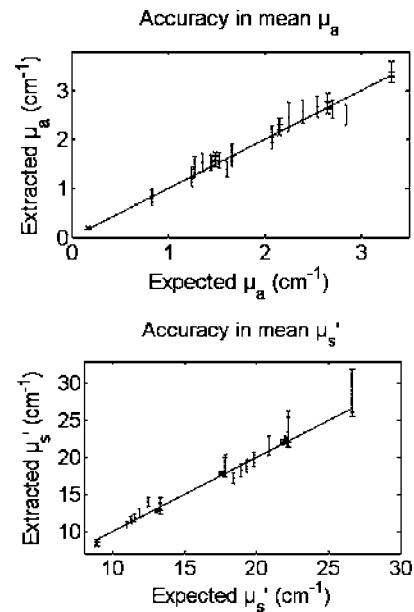Fig. 2. Extraction accuracy for all reference–target combinations within sets SA_Hb_a, SA_Hb_b, and SA_Cr. Averages and standard deviation are calculated over all reference phantoms for each target within a phantom set. The black line is the line of perfect agreement.

TABLE VI
EXTRACTION ACCURACY (AVERAGE PERCENT ERROR ± STANDARD DEVIATION) FOR ALL REFERENCE–TARGET COMBINATIONS FOR SINGLE-ABSORBER PHANTOMS

	SA_Hb_a-Hb additions	SA_Hb_b-Scatterer additions	SA_Cr-Cr additions
Mean error in μ_a (%)	9.08 ± 11.9	9.68 ± 10.3	7.84 ± 7.2
Mean error in μ_s' (%)	5.30 ± 4.1	6.79 ± 7.1	1.95 ± 1.5

instrument A with the 1.9-nm bandpass setting and probe A. The quantitative accuracy for wavelength-averaged extracted μ_a and μ_s' was determined for all reference–target phantom combinations and then averaged over all reference phantoms to produce the average percent error ± standard deviation within a phantom set. The percent errors are presented as absolute values. Fig. 2 shows the extracted versus expected wavelength-averaged μ_a and μ_s' for all phantoms in the three sets. Table VI shows the extraction accuracy for all reference–target combinations. The similarity in extracted optical parameters, regardless of the absorber, indicates the MC model's excellent adaptability to different absorbing species.

1) Choice of Reference Phantom: Fig. 3 shows error grids depicting the wavelength-averaged percent errors in extracted μ_a and μ_s' for all reference–target combinations within SA_Hb_a, SA_Hb_b, and SA_Cr. Each square represents a single reference–target combination; light gray squares are combinations in which the error is under 10%, medium gray squares are between 10% and 20% error, and black squares are greater than 20% error. White squares are combinations for which no phantom measurements were taken. For each scattering level, there are five possible absorber levels, which are indicated for S1. The dark black lines separate each scattering level. It is
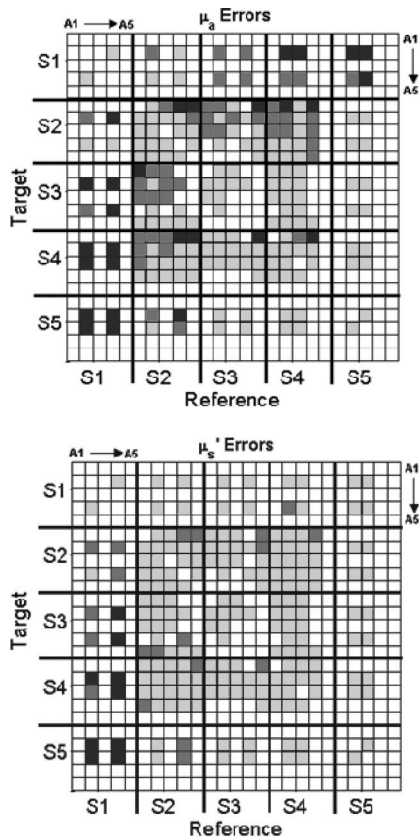
Fig. 3. Extraction accuracy in μ_a and μ_s' summarized over all reference–target combinations in SA_Hb_a, SA_Hb_b, and SA_Cr. The light gray blocks represent <10% error, medium gray blocks represent between 10%–20% error, and black blocks represent >20% error. Each of the absorber levels A1–A5 repeat for each scattering level S1–S5.

Fig. 4. Extraction accuracy of μ_a when (top) a low μ_s' reference is used for a high μ_s' target and (bottom) when a high μ_s' reference is used for a low μ_s' target.

TABLE VII
AVERAGE OPTICAL PROPERTIES (350–600 nm) FOR PHANTOMS CONTAINED IN MASTER REFERENCE SET

Phantom	Mean μ_a (cm^{-1})	Mean μ_s' (cm^{-1})
A1-S3	0.2	19.9
A1-S4	0.2	24.8
A2-S2	1.5	14.9
A2-S3	1.5	19.9
A2-S4	1.5	24.8
A2-S5	1.5	29.7
A3-S2	2.2	14.9
A3-S3	2.2	19.9
A3-S4	2.2	24.8
A3-S5	2.2	29.7
A4-S3	2.7	19.9

evident from the μ_a errors that the low-scattering phantoms are poor references for the high-scattering phantoms, and high-scattering phantoms are poor references for the low-scattering phantoms. There are also high errors seen in some instances where the A1 level is the target phantom. This could be explained by the choice of absorber levels, as A1 was much lower than that of any other levels. The μ_s' errors are uniformly lower than the μ_a errors, with the exception of the case where a low scattering reference is used for high-scattering target phantoms.

The quantitative accuracy of extracted μ_a was highly dependent on the choice of reference phantom. If a reference phantom from level S1 or S2 is used to extract the optical properties from a target in S3–S5, the μ_a is typically overestimated. Conversely, when a reference from S3 to S5 is used for a target in S1 or S2, μ_a is typically underestimated. This is demonstrated in Fig. 4.

Based on the errors from the single-absorber phantom studies, the reference phantoms that had lower than 10% average error in extracted μ_a over all available targets were, in order of ascending errors (absorber level–scattering level) A3–S3, A4–S3, A1–S3, A2–S3, A3–S5, A2–S5, A3–S4, A2–S4, A2–S2, A1–S4, and A3–S2. These 11 phantoms will be referred to as the master reference set, and their average optical properties are shown in Table VII.
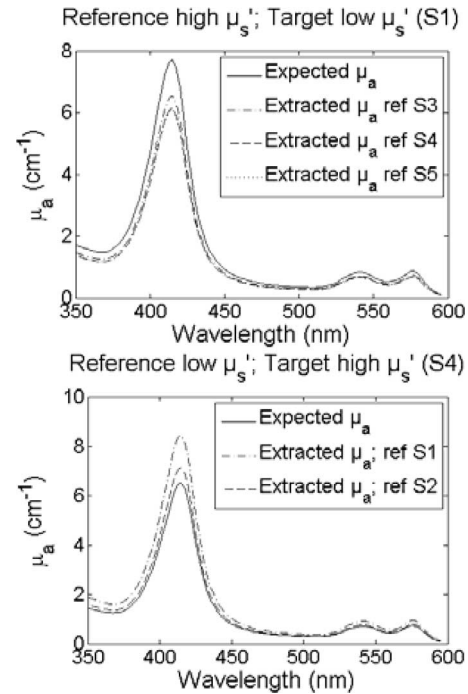
2) Different Instruments and Probes: Phantom sets SA_Hb_a and SA_Hb_b were tested using probe A and both instruments and probe B with Instrument B. For probe A and Instrument A, both the 1.9- and 10-nm bandpass settings were tested for SA_Hb_a. The average percent errors were calculated using references common to SA_Hb_a and SA_Hb_b from the master reference set—A3–S4, A2–S2, and A2–S4—for all ten target phantoms. There were no significant differences in μ_a or μ_s' for any instrument and probe combination for either phantom set using the 1.9-nm bandpass setting on instrument A. When the 10-nm bandpass setting was used, the μ_s' errors were similar, but there was a significant increase in the μ_a errors. This indicates the increased accuracy in extracting the absorption coefficient when a narrow bandpass setting is used, possibly because the narrow bandpass enables Hb spectral features to be captured. The errors are summarized in Table VIII.

TABLE VIII
EXTRACTION ACCURACY (AVERAGE PERCENT ERROR $\pm$ STANDARD DEVIATION) USING A3–S4, A2–S2, AND A2–S4 AS REFERENCES FOR ALL TARGETS COMPARED ACROSS DIFFERENT INSTRUMENTS AND PROBES FOR SA_HB_A AND SA_HB_B

	SA_Hb_a			
	Probe A Instrument B	Probe B Instrument B	Probe A Instrument A	
			1.9 nm bandpass	10 nm bandpass
Mean error in μ_a (%)	8.42 ± 11.3	4.66 ± 5.4	6.03 ± 5.9	23.20 ± 35.4
Mean error in μ_s' (%)	3.44 ± 2.1	5.32 ± 3.4	4.87 ± 3.4	3.18 ± 2.5
	SA_Hb_b			
Mean error in μ_a (%)	4.48 ± 4.9	3.94 ± 3.2	6.30 ± 6.4	-
Mean error in μ_s' (%)	4.21 ± 2.6	5.61 ± 3.7	4.27 ± 2.9	-

Fig. 6. Extraction accuracy of Hb concentration using references H1–H8 and all targets from Conc_Hb.

Fig. 7. Extraction accuracy of concentration of Hb (top) and Cr (bottom) in DA_HbCr when five references from PS1 measured on a different day were used for all targets.
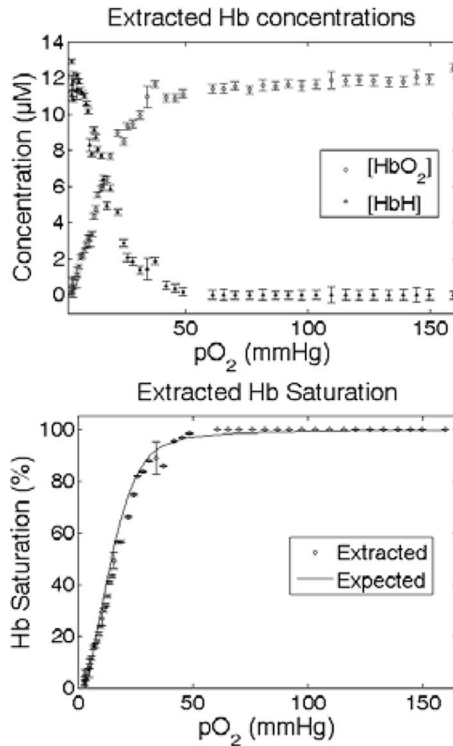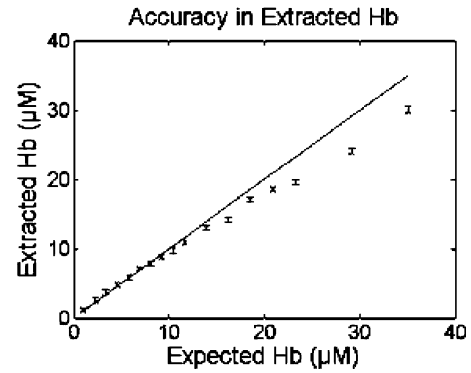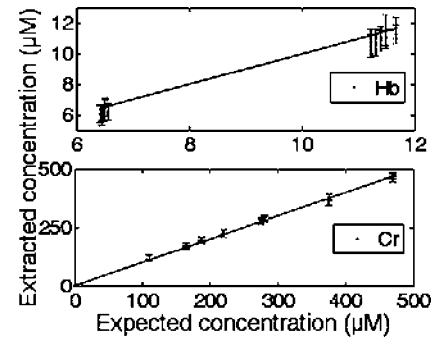

Fig. 5. Extracted HbO_2 and HbH as a function of measured pO_2 (top); extracted versus expected Hb saturation (bottom).

B. Hb Saturation Phantoms

The concentrations of HbO_2 and HbH were extracted for the Sat_Hb phantom using the two reference phantoms contained in the master reference set—A2–S2 and A3–S2. The extracted values are shown in Fig. 5 (top). The Hb saturation measurements were validated using the same method reported in [31], where n and p_{50} were calculated via fitting to the Hill equation (Hb saturation $= pO_2^n/(pO_2^n + p_{50}^n)$) over the range of 20%–80% Hb saturation. The expected Hb saturation [30] was calculated

for the range of measured oxygen partial pressures at $T = 24\,^{\circ}\text{C}$ and pH 6.94. The extracted and expected Hb saturations are shown in Fig. 5 (bottom). The expected value for n and p_{50} are 2.44 and 14.46 mmHg, respectively. The extracted values for n and p_{50} from our phantoms were 2.40 ± 0.05 and 16.28 ± 0.25 mmHg, respectively, indicating excellent agreement with the predicted values.

C. Hb Concentration Phantoms

The quantitative accuracy in extracting Hb concentration was tested using three reference levels contained in the master phantom set—A3–S4, A2–S4, and A1–S4, corresponding to phantoms H1 through H8 (see Table IV)—and all targets in Conc_Hb. Fig. 6 shows the extraction accuracy. The average percent error in extracted μ_a over these reference–target combinations was $9.80\% \pm 8.2\%$, and for μ_s', it was $7.68\% \pm 6.3\%$.

D. Double-Absorber Phantoms

The quantitative accuracy in extracted concentrations of Hb and Cr in double-absorber phantoms was tested to assess the ability to extract information about multiple absorbers using the inverse MC algorithm. The effect of having reference–target phantoms from different days was tested using the five phantoms from SA_Hb_a contained in the master reference set—A3–S4, A2–S2, A2–S4, A1–S4, and A3–S2. Fig. 7 shows the expected concentration versus extracted concentration for Hb

(upper panel) and Cr (lower panel). The average percent errors in extracting the concentrations of Hb and Cr were 7.69% ± 3.6% and 4.40% ± 4.0%, respectively. This shows excellent ability to extract concentrations when two absorbing species are present using reference phantoms from a different day.

IV. DISCUSSION

We demonstrate the feasibility for our MC model of light transport to accurately extract optical properties of tissue-mimicking phantoms in the near-UV to visible wavelength range, independent of instrument and probe for multiple absorbers and a large range of Hb saturations and concentrations. The quantitative accuracy was enhanced when an instrumentation setup with a 1.9-nm spectral bandpass compared to a 10-nm spectral bandpass was used. The accuracy of μ_a was impacted by the bandpass but μ_s' was not. One potential explanation of the increased accuracy of μ_a with a smaller bandpass is that the structural features of Hb can be captured more effectively. Based on the phantom absorber and scattering levels used in these experiments, we selected 11 phantoms to comprise the master reference set—A3–S3, A4–S3, A1–S3, A2–S3, A3–S5, A2–S5, A3–S4, A2–S4, A2–S2, A1–S4, and A3–S2. These phantoms spanned from the A1 to A4 absorber level and the S2 to S5 scattering level.

The lowest errors in μ_a were demonstrated when phantoms with a particular scattering level were used as references for target phantoms with the same scattering level. Specifically, phantoms from S1 or S2 best extracted the μ_a and μ_s' from phantoms from the same levels, and likewise the same was seen for scattering levels S3–S5. Additionally, it was determined from the Hb concentration phantoms that having reference phantoms with absorber concentrations close to the target phantoms was advantageous. Phantoms with the highest concentration of Hb (35.2 μM) were only able to accurately extract (under 20% average error) μ_a from target phantoms with similarly high concentrations (21.1 μM and higher). However, phantoms from the master reference set, which had lower concentrations, were able to accurately extract μ_a from all target phantoms, even those with high concentrations of Hb. The underestimation of Hb concentration as a function of concentration may be attributed to the differences in the signal levels between the low- and high-absorption phantoms. Because the integration time within the experiment was not varied, as the concentration of Hb increased, the signal level decreased. This signal mismatch may have caused an amplification of the noise and thus the errors. A mismatch in scattering could also have contributed to the errors in μ_a as the scattering level decreased from S4 to S2, due to the addition of the absorber. Further work would be required to develop a method to correct the mismatch of scattering and absorption between the reference and target phantoms or tissues.

We validated the accuracy of Hb saturation values obtained from extracted HbO_2 and HbH concentrations in hemoglobin phantoms. The values for the Hill coefficient and partial pressure of oxygen at which Hb is 50% saturated obtained from our phantom studies were in excellent agreement with expected values. We showed a large range of applicability for our algo-

rithm to extract concentrations of Hb and Cr in double-absorber phantoms, using single-absorber reference phantoms measured on a different day. By taking reference measurements on a different day before or after the target measurements and simply keeping track of daily system throughput, the time spent taking the target measurement set is reduced. Additionally, by having a set of reference phantoms to use for all samples within a clinical study, for example, there is a reduction in the experimental bias that may arise from taking reference measurements on a daily basis. The phantom studies conducted here were modeled as homogenous mixtures. In tumors, the vasculature and degree of oxygenation are typically nonuniform. Additionally, necrosis in different areas of the tumor can affect scattering. Further phantom studies would be required to test the limitations of tumor heterogeneity on the MC model.

The results from these studies have implications on the inversions performed on clinical measurements. We showed the ability to extract information about multiabsorber phantoms using reference phantoms consisting of only one absorber, which is directly translatable to single-absorber phantoms being used as references for tissue measurements in the preclinical or clinical setting. While the exact optical properties of the tissue are not known, the ranges typically are known, and so we can use reference phantoms that have been shown to most accurately extract the optical properties from that range. For tissues with low scattering, we would want to use a reference with low scattering and vice versa for the tissue with high scattering. The results from these phantom studies thus can serve as a set of guidelines for parameters used in the collection and postprocessing of clinical spectra that may potentially improve standard of care through increased quantitative accuracy.

REFERENCES

[1] C. Zhu, G. M. Palmer, T. M. Breslin, F. Xu, and N. Ramanujam, "Use of a multiseparation fiber optic probe for the optical diagnosis of breast cancer," *J. Biomed. Opt.*, vol. 10, no. 2, pp. 024032-1–024032-13, Mar./Apr. 2005.

[2] R. R. Alfano, B. B. Das, J. Cleary, R. Prudente, and E. J. Celmer, "Light sheds light on cancer—Distinguishing malignant tumors from benign tissues and tumors," *Bull. NY Acad. Med.*, vol. 67, no. 2, pp. 143–150, Mar./Apr. 1991.

[3] I. J. Bigio, S. G. Bown, G. Briggs, C. Kelley, S. Lakhani, D. Pickard, P. M. Ripley, I. G. Rose, and C. Saunders, "Diagnosis of breast cancer using elastic-scattering spectroscopy: Preliminary clinical results," *J. Biomed. Opt.*, vol. 5, no. 2, pp. 221–228, Apr. 2000.

[4] V. Chernomordik, D. W. Hattery, D. Grosenick, H. Wabnitz, H. Rinneberg, K. T. Moesta, P. M. Schlag, and A. Gandjbakhche, "Quantification of optical properties of a breast tumor using random walk theory," *J. Biomed. Opt.*, vol. 7, no. 1, pp. 80–87, Jan. 2002.

[5] G. M. Palmer, C. Zhu, T. M. Breslin, F. Xu, K. W. Gilchrist, and N. Ramanujam, "Comparison of multiexcitation fluorescence and diffuse reflectance spectroscopy for the diagnosis of breast cancer (March 2003)," *IEEE Trans. Biomed. Eng.*, vol. 50, no. 11, pp. 1233–1242, Nov. 2003.

[6] T. M. Breslin, F. Xu, G. M. Palmer, C. Zhu, K. W. Gilchrist, and N. Ramanujam, "Autofluorescence and diffuse reflectance properties of malignant and benign breast tissues," *Ann. Surg. Oncol*, vol. 11, no. 1, pp. 65–70, Jan. 2004.

[7] G. M. Palmer, C. Zhu, T. M. Breslin, F. Xu, K. W. Gilchrist, and N. Ramanujam, "Monte Carlo-based inverse model for calculating tissue optical properties. Part II: Application to breast cancer diagnosis," *Appl. Opt.*, vol. 45, no. 5, pp. 1072–1078, Feb. 2006.

[8] C. Zhu, G. M. Palmer, T. M. Breslin, J. Harter, and N. Ramanujam, "Diagnosis of breast cancer using diffuse reflectance spectroscopy: Comparison of a Monte Carlo versus partial least squares analysis based feature

extraction technique," *Lasers Surg. Med.*, vol. 38, no. 7, pp. 714–724, Aug. 2006.

[9] B. Yu, E. S. Burnside, G. A. Sisney, J. M. Harter, C. Zhu, A. Dhalla, and N. Ramanujam, "Feasibility of near-infrared diffuse optical spectroscopy on patients undergoing image-guided core-needle biopsy," *Opt. Exp.*, vol. 15, no. 12, pp. 7335–7350, Jun. 2007.

[10] M. C. Skala, G. M. Palmer, K. M. Vrotsos, A. Gendron-Fitzpatrick, and N. Ramanujam, "Comparison of a physical model and principal component analysis for the diagnosis of epithelial neoplasias in vivo using diffuse reflectance spectroscopy," *Opt. Exp.*, vol. 15, no. 12, pp. 7863–7875, Jun. 2007.

[11] A. Cerussi, D. Hsiang, N. Shah, R. Mehta, A. Durkin, J. Butler, and B. J. Tromberg, "Predicting response to breast cancer neoadjuvant chemotherapy using diffuse optical spectroscopy," *Proc. Nat. Acad. Sci. USA*, vol. 104, no. 10, pp. 4014–4019, Mar. 2007.

[12] D. B. Jakubowski, A. E. Cerussi, F. Bevilacqua, N. Shah, D. Hsiang, J. Butler, and B. J. Tromberg, "Monitoring neoadjuvant chemotherapy in breast cancer using quantitative diffuse optical spectroscopy: A case study," *J. Biomed. Opt.*, vol. 9, no. 1, pp. 230–238, Jan./Feb. 2004.

[13] C. Zhou, R. Choe, N. Shah, T. Durduran, G. Yu, A. Durkin, D. Hsiang, R. Mehta, J. Butler, A. Cerussi, B. J. Tromberg, and A. G. Yodh, "Diffuse optical monitoring of blood flow and oxygenation in human breast cancer during early stages of neoadjuvant chemotherapy," *J. Biomed. Opt.*, vol. 12, no. 5, pp. 051903-1–051903-11, Sep./Oct. 2007.

[14] Q. Zhu, S. H. Kurtzma, P. Hegde, S. Tannenbaum, M. Kane, M. Huang, N. G. Chen, B. Jagjivan, and K. Zarfos, "Utilizing optical tomography with ultrasound localization to image heterogeneous hemoglobin distribution in large breast cancers," *Neoplasia*, vol. 7, no. 3, pp. 263–270, Mar. 2005.

[15] J. Lee, A. E. Cerussi, D. Saltzman, T. Waddington, B. J. Tromberg, and M. Brenner, "Hemoglobin measurement patterns during noninvasive diffuse optical spectroscopy monitoring of hypovolemic shock and fluid replacement," *J. Biomed. Opt.*, vol. 12, no. 2, pp. 024001-1–024001-8, Mar./Apr. 2007.

[16] G. Zonios, L. T. Perelman, V. Backman, R. Manoharan, M. Fitzmaurice, J. Van-Dam, and M. S. Feld, "Diffuse reflectance spectroscopy of human adenomatous colon polyps in vivo," *Appl. Opt.*, vol. 38, pp. 6628–6637, Nov. 1999.

[17] N. Ghosh, S. K. Mohanty, S. K. Majumder, and P. K. Gupta, "Measurement of optical transport properties of normal and malignant human breast tissue," *Appl. Opt.*, vol. 40, pp. 176–184, Jan. 2001.

[18] Y. Yang, E. J. Celmer, J. A. Koutcher, and R. R. Alfano, "UV reflectance spectroscopy probes DNA and protein changes in human breast tissues," *J. Clin. Laser Med. Surg.*, vol. 19, no. 1, pp. 35–39, Feb. 2001.

[19] T. J. Pfefer, L. S. Matchette, C. L. Bennett, J. A. Gall, J. N. Wilke, A. J. Durkin, and M. N. Ediger, "Reflectance-based determination of optical properties in highly attenuating tissue," *J. Biomed. Opt.*, vol. 8, no. 2, pp. 206–215, Apr. 2003.

[20] A. Amelink, H. J. Sterenborg, M. P. Bard, and S. A. Burgers, "In vivo measurement of the local optical properties of tissue by use of differential path-length spectroscopy," *Opt. Lett.*, vol. 29, no. 10, pp. 1087–1089, May 2004.

[21] M. G. Müller, T. A. Valdez, I. Georgakoudi, V. Backman, C. Fuentes, S. Kabani, N. Laver, Z. Wang, C. W. Boone, R. R. Dasari, S. M. Shapshay, and M. S. Feld, "Spectroscopic detection and evaluation of morphologic and biochemical changes in early human oral carcinoma," *Cancer*, vol. 97, no. 7, pp. 1681–1692, Apr. 2003.

[22] G. Palmer and N. Ramanujam, "Monte Carlo-based inverse model for calculating tissue optical properties. Part I: Theory and validation on synthetic phantoms," *Appl. Opt.*, vol. 45, no. 5, pp. 1062–1071, Feb. 2006.

[23] P. Thueler, I. Charvet, F. Bevilacqua, M. St Ghislain, G. Ory, P. Marquet, P. Meda, B. Vermeulen, and C. Depeursinge, "In vivo endoscopic tissue diagnostics based on spectroscopic absorption, scattering, and phase function properties," *J. Biomed. Opt.*, vol. 8, no. 3, pp. 495–503, Jul. 2003.

[24] R. Graaff, M. H. Koelink, F. F. M. de Mul, W. G. Zijlstra, A. C. M. Dassel, and J. G. Aarnousdse, "Condensed Monte Carlo simulations for the description of light transport," *Appl. Opt.*, vol. 32, no. 4, pp. 426–434, Feb. 1993.

[25] W. S. Rasband, *ImageJ*. Bethesda, MD: U. S. National Institutes of Health, 1997–2004.

[26] X. Ma, J. Q. Lu, R. S. Brock, K. M. Jacobs, P. Yang, and X. H. Hu, "Determination of complex refractive index of polystyrene microspheres from 370 to 1610 nm," *Phys. Med. Biol.*, vol. 48, no. 24, pp. 4165–4172, Dec. 2003.

[27] Y. Yang, E. J. Celmer, J. A. Koutcher, and R. R. Alfano, "DNA and protein changes caused by disease in human breast tissues probed by the Kubelka–Munk spectral functional," *Photochem. Photobiol.*, vol. 75, no. 6, pp. 627–632, Jun. 2002.

[28] S. Prahl. (2005). Mie Scattering Program. [Online]. Oregon Med. Laser Center. Available: http://omlc.ogi.edu/software/mie/index.html

[29] W.-F. Cheong, *Optical–Thermal Response to Laser-Irradiated Tissue*. New York: Plenum, 1995.

[30] G. Kelman, "Digital computer subroutine for the conversion of oxygen tension into saturation," *J. Appl. Physiol.*, vol. 21, no. 4, pp. 1375–1376, Jul. 1966.

[31] E. L. Hull and T. H. Foster, "Noninvasive near-infrared hemoglobin spectroscopy for in vivo monitoring of tumor oxygenation and response to oxygen modifiers," *Proc. SPIE*, vol. 2979, pp. 355–364, 1997.

Authors' photographs and biographies not available at the time of publication.